Statistical-mechanical predictions and Navier-Stokes dynamics of two-dimensional flows on a bounded domain

H. Brands
KNMI (Netherlands Meteorological Institute), P.O. Box 201, 3730 AE De Bilt, The Netherlands

S. R. Maassen* and H. J. H. Clercx
Eindhoven University of Technology, P.O. Box 513, 5600 MB Eindhoven, The Netherlands

(Received 24 November 1998)

In this paper the applicability of a statistical-mechanical theory to freely decaying two-dimensional (2D) turbulence on a bounded domain is investigated. We consider an ensemble of direct numerical simulations in a square box with stress-free boundaries, with a Reynolds number that is of the same order as in experiments on 2D decaying Navier-Stokes turbulence. The results of these simulations are compared with the corresponding statistical equilibria, calculated from different stages of the evolution. It is shown that the statistical equilibria calculated from early times of the Navier-Stokes evolution do not correspond to the dynamical quasistationary states. At best, the global topological structure is correctly predicted from a relatively late time in the Navier-Stokes evolution, when the quasistationary state has almost been reached. This failure of the (basically inviscid) statistical-mechanical theory is related to viscous dissipation and net leakage of vorticity in the Navier-Stokes dynamics at moderate values of the Reynolds number. [S1063-651X(99)00508-5]

PACS number(s): 47.32.Cc, 47.27.Eq, 05.20.−y

I. INTRODUCTION

The formation of large-scale vortices in (quasi-)two-dimensional (2D) turbulence has been studied extensively in laboratory experiments [1–4] and in numerical simulations [5–7]. For sufficiently high Reynolds numbers, the flow eventually organizes in one large-scale structure, which is stable and stationary, apart from weak dissipative effects. Several authors have applied the principles of statistical mechanics to predict the form of these large-scale quasistationary structures. This approach was initiated by Onsager [8], who qualitatively predicted the appearance of coherent structures by considering a system of point vortices. Joyce and Montgomery [9] presented a general equation, known as the sinh-Poisson equation, for the statistical equilibrium of a point vortex system. Both Miller [10] and Robert and Sommeria [11] independently derived an alternative equation for the statistical equilibrium of an inviscid 2D fluid on the basis of a patchwise discretization of the continuous field. The aim of the present paper is a discussion of the applicability of this statistical theory of vortex patches to freely decaying 2D turbulence on a bounded domain, with Reynolds numbers comparable to those in laboratory experiments.

In several publications, statistical-mechanical predictions based on a patchwise discretization have been compared with the results of direct numerical simulations. A remarkably good agreement was found in a numerical simulation of the time evolution of a periodically continuated shear layer [12], and in the study of an isolated vortex merger [13]. However, a high Reynolds-number simulation of Navier-Stokes dynamics on a doubly periodic domain has shown that for an initially small-scale vorticity field, small but finite dissipation leads to limited predictability: the global form of the final, quasistationary vortex can be predicted from the initial conditions, but the details are only captured if the equilibrium is derived from the flow field after a few eddy turnover times [14]. Furthermore, laboratory experiments in a magnetized plasma column [4] and equivalent Navier-Stokes simulations have shown that for isolated, large-scale initial vorticity fields, the statistical theory applies only when it is restricted to a subdomain, because the time evolution is not globally ergodic in these cases [15]. Notwithstanding these limitations, the general conclusion from these comparisons is that the statistical predictions match the observed structures reasonably well in the case of a periodic or infinite domain.

However, laboratory experiments with realistic fluid flows are performed in finite containers with physical boundaries [2,3]. Since the quasistationary states emerging in such experiments usually fill the whole domain, the shape of these structures depends on the geometry of the container. Solutions of the various statistical-mechanical theories, based on either point vortices or vortex patches, have been investigated systematically for the case of a bounded domain. Both Pointin and Lundgren [16] and Ting, Chen, and Lee [17] calculated maximum entropy solutions of the sinh-Poisson equation on various bounded domains. Statistical equilibria for bounded fluids based on a patchwise discretization were calculated by Jüttner, Thess, and Sommeria [18] for a class of initial conditions consisting of isolated vortex patches, and by Chavanis and Sommeria [19] for initial conditions satisfying the so-called strong-mixing conditions. Several authors [3,18–20] have tried to relate these statistical solutions based on a patchwise discretization to experimental observations or numerical simulations, with varying success. For example, Marteau, Cardoso, and Tabeling [3] concluded that the calculated equilibria do not match experimentally observed qua-

*Author to whom correspondence should be addressed. Electronic address: S.R.Maassen@fdl.phys.tue.nl

sistationary structures in thin layers of electrolyte (with Re $\approx$1000), whereas a numerical simulation of the same experiment (approximated by a purely 2D system with stress-free boundaries and Re$\approx$3000) lead to the opposite conclusion [20]. Altogether, the applicability of the statistical-mechanical theory of vortex patches to finite domain fluid flows is still controversial.

The main problem in comparing statistical-mechanical equilibria with Navier-Stokes simulations in closed geometries is the appropriate choice of boundary conditions. In the various (basically inviscid) statistical-mechanical theories, the boundaries are completely determined by the impermeability condition (no in or outflow), whereas the second-order derivatives in the viscous term of the Navier-Stokes equation require a second boundary condition. Numerical simulations of decaying 2D turbulence in circular [21] and square [22,23] containers have shown that, for moderate values of the Reynolds number (Re$\lesssim$2000) the choice of this second boundary condition (either no-slip or stress-free) influences the topology of the quasistationary state. In the physically most relevant case of no-slip boundaries, strong vorticity sheets emerge in the viscous boundary layers, which detach from the boundaries and interact with the flow in the interior of the domain. This process of creation and detachment of viscous boundary layers cannot be taken into account in statistical-mechanical equilibria. Therefore, it is unlikely that statistical theories correctly predict the quasistationary states observed in laboratory experiments and numerical simulations with no-slip boundaries at moderate values of Re [22]. The best one can hope is that for sufficiently high Reynolds numbers, the statistical prediction corresponds to the interior flow structure, i.e., excluding the boundaries. However, such high Reynolds number computations are not possible with present state-of-the-art numerical techniques for flows with no-slip boundaries. Since shear dominated boundary layers do not occur in simulations with stress-free boundary conditions [22], such simulations seem to be better suited for comparison between statistical predictions and Navier-Stokes dynamics with moderate Reynolds numbers.

In this paper we reconsider the applicability of the statistical-mechanical theory of vortex patches in the case of a bounded domain. In particular, we present the results of an ensemble of Navier-Stokes runs in a square box with stress-free boundaries (Sec. II) and the corresponding statistical equilibria, calculated from different stages of the evolution (Sec. III). The initial vorticity fields are small-scale, quasiturbulent, random distributions of vorticity. Although viscous effects cannot be neglected for such small-scale initial conditions [14], we have made this choice in order to avoid problems related to ergodicity and to make sure that the quasistationary states are the results of unbiased turbulent relaxation.

II. NAVIER-STOKES DYNAMICS

A. Numerical method

In this section the results of a numerical experiment, based on simulations of the 2D incompressible Navier-Stokes equation, are presented. The experiment consists of an ensemble of runs, each with a different quasiturbulent initial condition. Formulated in terms of the velocity $\mathbf{v}=(u,v)$ and the vorticity $\omega=\hat{\mathbf{z}}\cdot\boldsymbol{\nabla}\times\mathbf{v}$, the equations of motion are

$$\frac{\partial\omega}{\partial t}+(\mathbf{v}\cdot\boldsymbol{\nabla})\omega=\frac{1}{\mathrm{Re}}\nabla^2\omega, \tag{1}$$

$$\nabla^2\mathbf{v}=\hat{\mathbf{z}}\times\boldsymbol{\nabla}\omega. \tag{2}$$

The Reynolds number is defined as $\mathrm{Re}=UW/\nu$, where U is the root of the mean-squared velocity of the initial flow field per unit surface, W is the half-width of the domain and ν is the kinematic viscosity of the fluid. All runs described in this paper are performed with Re=2000. The unit of time t is the time-independent eddy turnover time W/U.

The flow is confined to the square box $[-1,1]\times[-1,1]$ with boundary b by enforcing the impermeability condition

$$\hat{\mathbf{n}}\cdot\mathbf{v}|_b=0. \tag{3}$$

Note that, in the vorticity-stream function representation of model (1) and (2), condition (3) is equivalent to imposing $\psi|_b=\mathrm{const}$, where the stream function ψ is defined by the Poisson equation $\omega=-\nabla^2\psi$. In addition, we impose the flow to be stress-free at the boundary:

$$\hat{n}\cdot\nabla v_{\parallel}|_b=0, \tag{4}$$

where $v_{\parallel}$ is the component of the velocity parallel to the boundary. On a square domain, a combination of conditions (3) and (4) yields

$$\omega|_b=0, \tag{5}$$

which will be used as a boundary condition for the vorticity equation (1).

Equations (1)–(5) are solved numerically with a 2D Chebyshev pseudospectral method. Using Cartesian coordinates $\mathbf{r}=(x,y)$, the vorticity and both components of the velocity are expanded in a double truncated series of Chebyshev polynomials; for example, $\omega(x,y,t)=\sum_{n=0}^{N}\sum_{m=0}^{N}\omega_{nm}(t)T_n(x)T_m(y)$, with $T_n(x)=\cos(n\theta)$ and $\theta=\cos^{-1}(x)$. The numerical integration is performed in spectral space, except for the evaluation of the nonlinear terms, which are calculated in physical space using fast Fourier transformations. The time integration is based on the second-order accurate semi-implicit Adams-Bashforth-Crank-Nicolson scheme. Further details of the numerical procedure can be found in [22–24].

An ensemble of 16 independent, quasiturbulent, initial conditions is constructed in the following way. For each member of the ensemble the first 65×65 Chebyshev coefficients of both components of the velocity are drawn randomly from a zero-mean Gaussian distribution. The variance σ_{nm} of the initial velocity spectrum is chosen as

$$\sigma_{nm}^2=\frac{nm}{[1+(\frac{1}{8}n)^4][1+(\frac{1}{8}m)^4]}\quad\text{for } 0\leqslant n,\ m\leqslant 64, \tag{6}$$

and $\sigma_{nm}=0$ for $n,\ m\geqslant 65$. Subsequently, the resulting velocity field is multiplied by smoothing functions $f(x)$ and $f(y)$ in order to enforce $\mathbf{v}(\mathbf{r},t=0)=0$ at the boundaries ($f(x)$

$=[1-\exp\{-\beta(1-x^2)^2\}]$ with $\beta=100$). The resulting velocity field $\mathbf{v}(\mathbf{r},0)$ is normalized such that the L^2 norm of the velocity field per unit surface is equal to one. It should be noted that the initialization procedure described above leads to velocity fields with $\nabla\cdot\mathbf{v}\neq 0$, which are physically irrelevant. Although a divergence-free flow field with stress-free boundary conditions is enforced during the first time integration step, a short transient phase occurs in which a realistic physical situation is reached. Therefore, the field at $t=1$ will be considered as the physical initial condition of the flow evolution.

The time integration is sensitive to the number of Chebyshev modes used in the expansion. It is found that for this particular type of initial conditions and this particular value of the Reynolds number (Re=2000), $N=288$ Chebyshev modes in each direction is sufficient to resolve the smallest scales of the flow field: increasing this number does not change the results of the integration during the first 300 eddy turnover times. Since numerical simulations of flows with nonperiodic boundary conditions are computationally much more expensive then the doubly periodic case, the hardware necessary to perform well-resolved simulations with higher Reynolds numbers was not available.

During the numerical computations, several integrals are calculated, such as the total energy E, the net circulation Γ, and the nth moment of the vorticity Γ_n (with, in particular, the enstrophy Γ_2). These quantities are defined, respectively, as

$$E(t)=\frac{1}{2}\int \mathbf{v}(\mathbf{r},t)^2 d\mathbf{r}, \tag{7}$$

$$\Gamma(t)=\int \omega(\mathbf{r},t)d\mathbf{r}, \tag{8}$$

$$\Gamma_n(t)=\int \omega^n(\mathbf{r},t)d\mathbf{r}. \tag{9}$$

Due to the random initialization, the values of the circulation at $t=1$ are small in each realization and zero on average.

B. Results of the numerical simulations

The most remarkable observation in the numerical experiment is that the different integrations do not evolve towards the same equilibrium state, although their initial conditions are statistically equivalent. Roughly speaking, the different quasistationary states that are found belong to two topology classes: dipoles and monopoles. The emergence of these structures is illustrated in Figs. 1 and 2, respectively, which contain snapshots of the evolving vorticity fields of two typical runs. For $t\lesssim 15$ [cf. Figs. 1(a)–1(c) and Figs. 2(a)–2(c)], the global dynamics of all simulations is characterized by the formation of coherent structures (monopoles, dipoles, and, occasionally, tripoles) and the appearance of thin vorticity-gradient sheets in regions of high strain between the vortices and between the vortices and the walls. For $15\lesssim t\lesssim 45$, the flow organizes into a large structure. At this point the differences between the runs become evident: in Fig. 1 an almost symmetric dipole emerges [Figs. 1(d) and 1(e)] that remains present until at least $t=100$, while in Fig. 2, initially a very

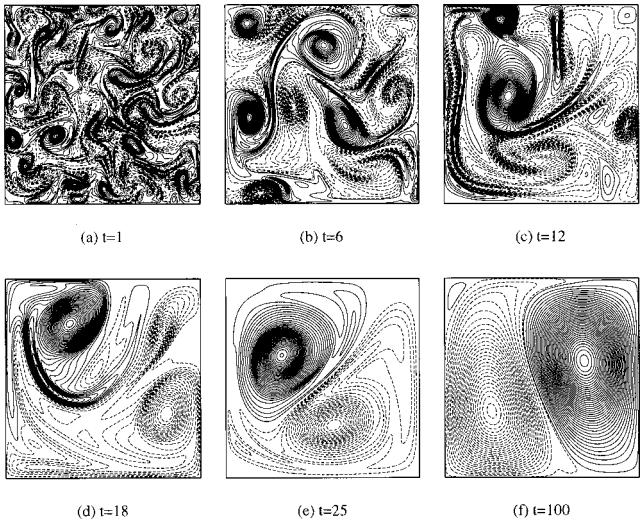

FIG. 1. Navier-Stokes time evolution of the vorticity field, for a typical run in which a relatively symmetric dipole is formed. Dashed contours represent positive vorticity, solid contours represent negative vorticity. The contour intervals are (a) 2, (b) 0.5, (c) 0.25, (d) 0.2, (e) 0.1, and (f) 0.05.

asymmetric dipole is formed, which transforms into a monopole at later times [cf. Figs. 2(d) and 2(e)]. For $t\gtrsim 45$, the flow dynamics is essentially determined by viscous dissipation, a regime that is not part of the present study. Still, it is interesting to see that the dipolar structure does not stay in the same position, but performs a slow rotating motion. For instance, between Figs. 1(e) and 1(f), the dipole has rotated a bit more than 90° clockwise.

In our numerical experiment, a majority of runs (12 out of 16) evolved towards a dipolar structure, such as shown in Fig. 1, whereas the monopolar structure, such as the one formed in Fig. 2, was obtained in only four cases. This division in terms of topology is, however, quite rough. The dipolar structures, in fact, range from very symmetric dipoles

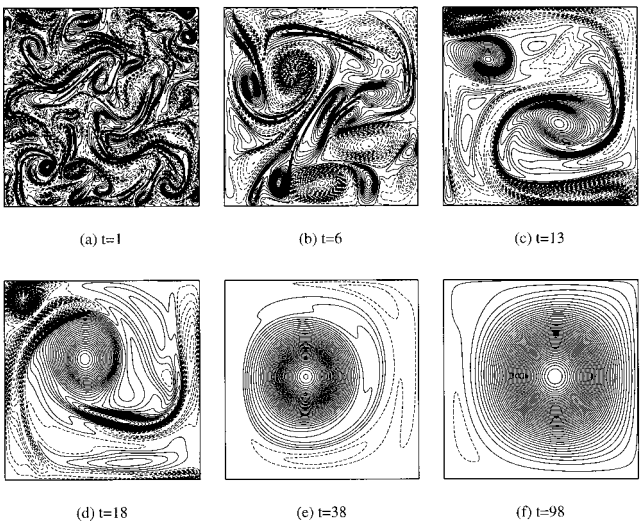

FIG. 2. Navier-Stokes time evolution of the vorticity field, for a typical run in which a monopole is formed. Dashed contours represent positive vorticity, solid contours represent negative vorticity. The contour intervals are (a) 2, (b) 0.5, (c) 0.25, (d) 0.2, (e) 0.15, and (f) 0.05.

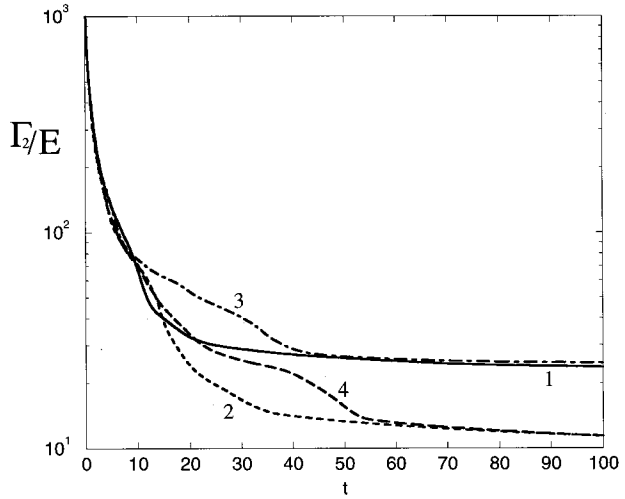

FIG. 3. Time evolution of the ratio Γ_2/E for four different runs. Curves 1 and 2 correspond to the runs shown in Figs. 1 and 2, respectively.

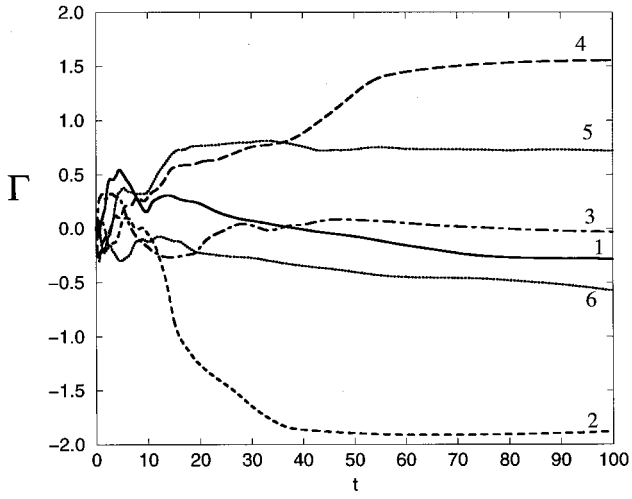

FIG. 4. The net circulation Γ plotted vs time t for six different runs. Curves 1 and 2 correspond to the runs shown in Figs. 1 and 2, respectively.

to cases where one of the vortices is substantially stronger than the other one. Once the dipole has been formed, the weaker vortex is often more strongly dissipated near the walls and the dipole becomes more and more asymmetric. In fact, the monopole formation shown in Fig. 2 can be regarded as an extreme realization of the asymmetric case: the small positive vortex in the upper left corner of Fig. 2(d) can be regarded as the weaker part of an asymmetric dipole. The small vortex keeps rotating around its negative counterpart, until at $t \simeq 35$ it is torn apart and distributed in a ring of positive vorticity [Fig. 2(e)].

The different time scales for dipole and monopole formations are clearly illustrated in Fig. 3, where the ratio of enstrophy and energy Γ_2/E is drawn. Since $\Gamma_2/E \sim k^2$, with k the dominant wave number of the energy spectrum, this ratio reflects the scale that dominates the vorticity field. Curves 1 and 2 correspond to the dipole and monopole formations shown in Figs. 1 and 2, respectively. The curve of the dipole approaches its minimum value (largest scale) already at $t \approx 25$, whereas the curve of the monopole formation approaches its (much lower) minimum at $t \approx 40$. Curve 3 reflects the very late emergence of another symmetric dipole (at $t \approx 40$), and curve 4 corresponds to a run in which a very asymmetric dipolar structure is formed around $t \simeq 25$. In this latter case one of the vortices is weakened by dissipation near the boundary until a monopolar structure remains at $t \simeq 55$. We expect that in the very late time viscous stage of the evolution ($t > 300$) monopoles will be formed in all runs, since this structure is the viscous eigenmode solution with the lowest damping rate [2,22,23,25].

Another characteristic difference between the decay scenarios presented in Figs. 1 and 2 is the time evolution of the total circulation Γ, defined in Eq. (8). In contrast to flows with no-slip or periodic boundaries, Γ is not a conserved quantity in a box with stress-free boundary conditions. Spatial integration of the Navier-Stokes equation (1) yields

$$\frac{d\Gamma}{dt} = \frac{1}{\mathrm{Re}} \oint ds \hat{\mathbf{n}} \cdot \boldsymbol{\nabla} \omega(\mathbf{r},t), \tag{10}$$

which implies that vorticity can diffuse through the boundaries. Figure 4 shows the time evolution of the net circulation for six different runs, including the dipole formation of Fig. 1 (curve 1) and the monopole formation of Fig. 2 (curve 2). It appears that for the almost symmetric dipole formations (curves 1, 3, and 6 in Fig. 4), positive and negative vorticity leak through the boundary in more or less equal amounts, whereas a symmetry breaking between positive and negative vorticity occurs in the cases where an asymmetric dipole (curve 5) or a monopole (curves 2 and 4) is formed. Defining the total positive and negative circulations $\Gamma^{\pm} = \int \omega^{\pm}(\mathbf{r},t) d\mathbf{r}$, with $\omega^{+} > 0$ and $\omega^{-} < 0$, respectively, this symmetry breaking is clearly illustrated in Fig. 5, where Γ^{+} and Γ^{-} are drawn for the two runs shown in Fig. 1 (solid curves) and Fig. 2 (dashed curves). The curves corresponding to the dipole formation stay relatively close to each other, but the curves corresponding the monopole formation start to diverge at about $t = 10$, leading to a strong decrease of the net circulation Γ (curve 2 in Fig. 4). Thus we can relate the value of Γ to the asymmetry of the dipolar state that emerges: for positive Γ, the positive vortex is stronger than the negative one, and vice versa.

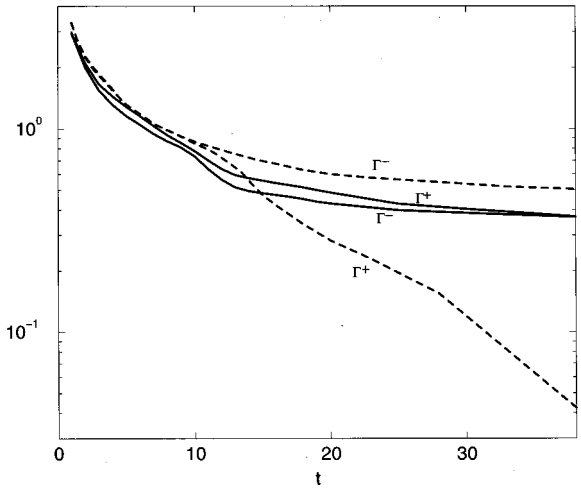

FIG. 5. Decay of the total positive (Γ^+) and negative (Γ^-) circulation for the dipole formation shown in Fig. 1 (solid lines) and the monopole formation shown in Fig. 2 (dashed lines).

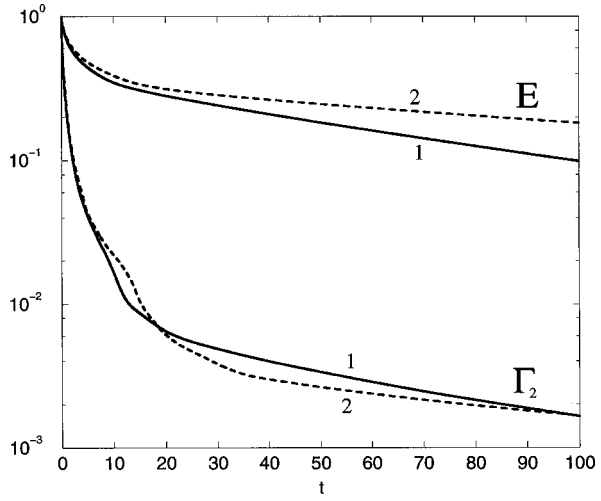

FIG. 6. Normalized energy E/E_0 and enstrophy $\Gamma_2/(\Gamma_2)_0$ plotted vs time t for the dipole formation shown in Fig. 1 (solid lines) and the monopole formation shown in Fig. 2 (dashed lines).

Since the numerical simulations are performed with a moderate value of the Reynolds number, viscous dissipation in the Navier-Stokes dynamics induces a significant decay of the normalized energy E/E_0 and enstrophy $\Gamma_2/(\Gamma_2)_0$ as illustrated in Fig. 6. Apart from decreasing the kinetic energy, viscous dissipation leads to rapid changes in the vorticity distribution in the early stages of the flow evolution. Figure 7(a) displays the fraction of the domain area (g) with a certain vorticity level (σ) for the run shown in Fig. 1 at $t=1$, 5, and 10. In this initial stage of the flow evolution, small-scale structures are efficiently dissipated, while high-value vorticity concentrates in isolated vortex structures. This leads to a vorticity distribution that is more sharply peaked around zero, as can be inferred from Fig. 7(a). The shape of the vorticity distribution is conveniently represented by the kurtosis $K=\Gamma_4/(\Gamma_2)^2$. Figure 7(b) displays the time evolution of kurtosis K, divided by its initial value K_0, for the two simulations considered in Fig. 1 (solid line) and Fig. 2 (dashed line). The initial growth of K is due to the evolution towards a more sharply peaked vorticity distribution, as shown in Fig. 7(a). In the final stages of the evolution, the flow dynamics is dominated by viscous dissipation of the large-scale vortex, which leads to a decrease of K. Therefore, at the point where K reaches its maximum value, the nonlinear evolution of the flow is basically depleted. In most cases we have found that shortly after this time, the ratio Γ_2/E becomes constant, indicating that the formation of the quasistationary state is completed [cf. curves 1 and 2 in Figs. 3 and 7(b)].

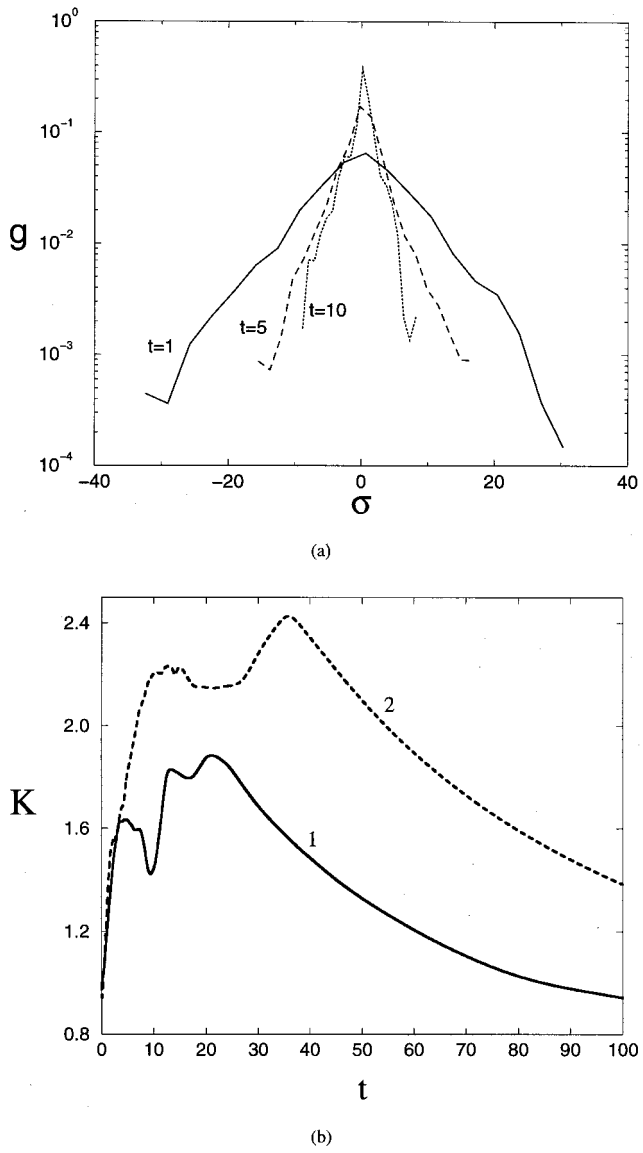

FIG. 7. (a) Vorticity distributions corresponding to the run shown in Fig. 1, plotted at three different times and (b) the kurtosis K plotted vs time t for the dipole formation shown in Fig. 1 (solid lines) and the monopole formation shown in Fig. 2 (dashed lines). The point where K reaches its maximum value can be identified with the emergence of the quasistationary state (cf. Fig. 3).

III. STATISTICAL-MECHANICAL PREDICTIONS

In this section the results of the Navier-Stokes simulations described in Sec. II are compared with predictions based on a statistical-mechanical theory for 2D turbulence, derived by Miller [10] and Robert and Sommeria [11]. Firstly, in Sec. III A we briefly describe the basic principles of this theory, based on a patchwise discretization of the continuous flow field, and present the equations defining the corresponding statistical equilibria. In Sec. III B the statistical-mechanical equilibria calculated from the initial conditions (at $t=1$) of the ensemble of Navier-Stokes simulations are presented and compared with the analytical solutions obtained by Chavanis and Sommeria in a linearized limit of the theory [19]. Finally, in Sec. III C it is shown how the statistical predictions change when the input vorticity fields are chosen from later times in the Navier-Stokes evolution.

A. Entropy maxima of the vortex patch model

The statistical-mechanical theory considered in this paper was derived on the basis of the inviscid Euler equation [10,11]. Inviscid (or high Reynolds number) flow dynamics is characterized by the development of very complex, thin vorticity filaments. A deterministic description of a perfectly inviscid flow, where these filaments are not dissipated,

would, therefore, require a rapidly increasing amount of information as time goes on. The idea of a statistical theory is to give up the deterministic description and introduce a probabilistic one. Therefore, the exact knowledge of the fine-grained, or microscopic, vorticity field $\omega(\mathbf{r})$ is replaced by the probability density $\rho(\mathbf{r},\sigma)$ of finding the vorticity value σ at position $\mathbf{r}$ [11]. Once the probability function is introduced, one can consider the locally averaged, or macroscopic, vorticity field $\overline{\omega}(\mathbf{r})=\int\sigma\rho(\mathbf{r},\sigma)d\sigma$. Generally, there are different microscopic vorticity fields that correspond to one macroscopic structure. The statistical equilibrium is defined as the macroscopic vorticity field that corresponds to the largest number of microscopic fields.

Counting the number of microscopic realizations corresponding to the same macroscopic structure leads to the definition of the mixing entropy:

$$S=-\int\rho(\mathbf{r},\sigma)\ln\rho(\mathbf{r},\sigma)d\sigma d\mathbf{r}. \tag{11}$$

If ergodicity is assumed, the most probable state is defined by the maximum of the entropy (11) for fixed values of the inviscid invariants, such as the energy E and the different moments of the vorticity Γ_n. The energy (7) can be expressed in terms of the macroscopic vorticity field and stream function (defined by $\overline{\omega}=-\nabla^2\psi$), and is taken to be conserved on the macroscopic level:

$$\frac{1}{2}\int\overline{\omega}\psi d\mathbf{r}=E_0, \tag{12}$$

where the subscript 0 refers to the (fixed) input value. The moments of the vorticity (9) are incorporated on a microscopic level by conserving the input vorticity distribution $g_0(\sigma)\equiv(1/V)\int\delta(\sigma-\omega_0(r))d\mathbf{r}$ via

$$\frac{1}{V}\int\rho(\mathbf{r},\sigma)d\mathbf{r}=g_0(\sigma), \tag{13}$$

in which V is the domain area. This condition implies that the total area of fluid elements with a certain vorticity value σ is conserved in the microscopic description. Note that Eq. (13) does not imply the conservation of the moments Γ_n on the macroscopic level, as they are partly transferred into fine-grained vorticity fluctuations, which vanish in the local averaging. For example, the enstrophy Γ_2 of the (coarse-grained) statistical equilibrium is generally lower than its input value, while the circulation Γ is exactly conserved on both fine- and coarse-grained levels. This distinction between macroscopic and microscopic invariants coincides with the distinction between ''robust'' and ''fragile'' invariants in nearly inviscid flows [26]: when the viscosity $\nu\rightarrow 0$, the energy and the circulation become constants of the motion, whereas the conservation of higher-order inviscid invariants is destroyed by any infinitesimally small amount of viscosity. Therefore, one can argue that the statistical theory of vortex patches extends to weakly viscous flows, at least in a qualitative sense, although it is derived on the basis of the inviscid equations of motion.

Setting the constrained entropy variation to zero, one finds a well-defined relationship between the equilibrium, macroscopic, vorticity, and stream function [10,11], which we denote by a superscript $*$:

$$\omega^*(\mathbf{r})=\frac{\int\sigma e^{-\beta\sigma\psi^*(r)-\mu(\sigma)}d\sigma}{\int e^{-\beta\sigma\psi^*(r)-\mu(\sigma)}d\sigma}. \tag{14}$$

The values of the Lagrange multipliers β and $\mu(\sigma)$ are determined by the input values of the energy E_0 and distribution $g_0(\sigma)$ via constraints (12) and (13). The solutions to Eqs. (12)–(14) are stable statistical equilibria, provided that they are true maxima, and not minima or saddle points, of the entropy, which remains to be checked. Together with the Poisson equation,

$$\omega^*(\mathbf{r})=-\nabla^2\psi^*(\mathbf{r}), \tag{15}$$

Eqs. (12)–(14) completely define the spatial structure of the statistical equilibrium. The geometry of the domain determines the boundary condition for the Poisson equation. In the present case of a closed box we put $\psi^*(\mathbf{r})|_b=0$. Note that, contrary to the Navier-Stokes equation, Eqs. (12)–(15) do not require a boundary condition for the vorticity. Therefore, the statistical-mechanical equilibrium depends only on the geometry of the domain and the values of the input constraints E_0 and $g_0(\sigma)$; the theory does not account for no-slip nor stress-free boundary conditions.

Since, for general input parameters $g_0(\sigma)$ and E_0, Eqs. (12)–(15) cannot be solved analytically, the entropy maxima have to be determined numerically. For this purpose, we use an algorithm developed by Turkington and Whitaker [27]. The numerical treatment requires not only a spatial discretization of the fields, but also an approximation of the continuous vorticity distribution at a finite number of vorticity levels σ_k. This brings the infinite set (13) down to a finite number of constraints. In order to calculate the values of the distribution $g_0(\sigma_k)$, the corresponding vorticity field $\omega(\mathbf{r})$ is discretized on a grid of 65×65 equidistant points. Subsequently, the continuous vorticity distribution is approximated by 30 equidistant levels σ_k, ranging between the minimum and maximum values of $\omega(\mathbf{r})$. We have checked that the equilibria are not sensitive to these approximations: increasing the number of gridpoints or the number of vorticity levels does not change the results. The numerical value of E_0 can be calculated directly from the velocity field $\mathbf{v}(\mathbf{r})$ using Eq. (7).

B. Predictions from $t=1$

The statistical equilibria calculated on the basis of the values of E_0 and $g_0(\sigma)$ at $t=1$ in the Navier-Stokes simulations, are characterized by an approximately linear relation between vorticity and stream function for all runs. For example, Fig. 8(a) depicts the ω-ψ relation of the equilibrium calculated from the field shown in Fig. 1(a). Figure 8(b) shows the corresponding vorticity field: a negative vortex surrounded by a ring of positive vorticity. The monopolar structure of the statistical equilibrium turns out to be generic for this class of initial conditions. The sign of the core depends sensitively upon the specific realization: we have found about as many positive as negative monopoles. Obvi-

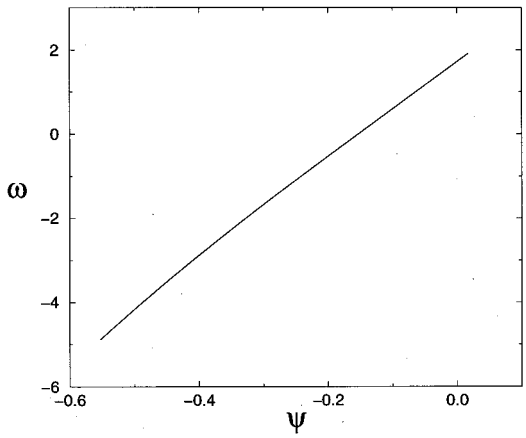

(a)

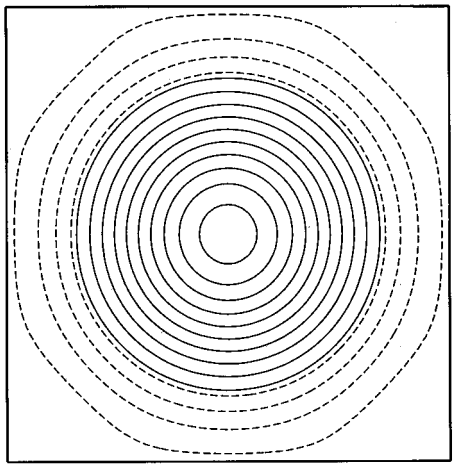

(b)

FIG. 8. ω-ψ relation (a) and vorticity field (b) of the statistical equilibrium calculated from the vorticity field shown in Fig. 1(a). Dashed contours represent positive vorticity, solid contours represent negative vorticity. The contour interval is 0.5. The shape of the vorticity field and the linear ω-ψ relation of this equilibrium are generic for all predictions at $t=1$.

ously, these statistical equilibria do not agree with the dipolar quasistationary states of the Navier-Stokes simulations presented in Sec. II.

The generality of the monopolar structure in the $t=1$ predictions can be understood by considering the so-called ''limit of strong mixing'', in which the entropy maximization is only weakly restricted by constraints (12) and (13). In this limit, the statistical equilibria are characterized by a linear relation between ω and ψ [19]. Since the statistical equilibria calculated from $t=1$ in our ensemble of simulations are characterized by such a linear ω-ψ relation, one can expect that the initial conditions used for these calculations lie in the strong-mixing regime. This property could have been inferred *a priori* from the abundance of small-scale structures in the initial conditions.

In Ref. [19] Chavanis and Sommeria presented a classification of such linearized solutions on a bounded domain. The authors show that the structure of the solutions in the linearized limit depends only upon a single parameter Λ, defined by

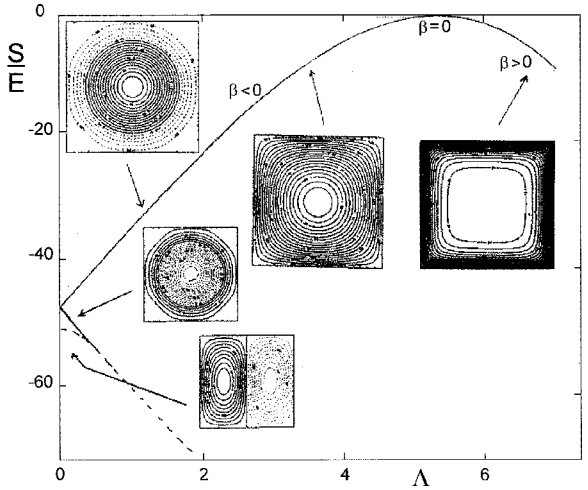

FIG. 9. The ratio S/E vs a control parameter $\Lambda(\Lambda^2=\Gamma^2/2E)$ for different statistical equilibria in a square box, obtained in the linearized approximation of the ω-ψ relation, calculated by Chavanis and Sommeria [19]. The two solid curves represent stable monopolar solutions of different sign (solid contours represent positive vorticity, dashed contours represent negative vorticity). Above a certain threshold, the negative monopole becomes unstable. The dashed curve represents dipolar solutions, which can be shown to be unstable for all values of Λ. We gratefully acknowledge P-H. Chavanis for providing this picture.

$$\Lambda=\frac{\Gamma}{\sqrt{2E}}. \tag{16}$$

Figure 9 displays a diagram of the ratio between entropy and energy S/E versus Λ, for three different solutions to the linearized equations in a square box. (We kindly thank Dr. P-H. Chavanis for providing this picture). In this diagram, solid curves represent stable solutions, and the dashed curve corresponds to unstable solutions. The solutions with negative Λ (i.e., $\Gamma<0$), not depicted in this figure, can be obtained from the positive Λ structures by reversing the signs of the vorticity and stream function.

For all the initial conditions of our ensemble, we found $|\Lambda|<0.2$. From the diagram depicted in Fig. 9 one can read that in this range both positive and negative monopoles are stable statistical equilibria in the linearized limit (solid lines). Only above a certain threshold ($|\Lambda|\approx 0.5$), the solution with the lowest entropy (a negative monopole when $\Lambda,\Gamma>0$ and a positive monopole when $\Lambda,\Gamma<0$) becomes unstable. This analysis of the linearized case is consistent with the numerical solutions of the full statistical-mechanical equations presented above, where indeed both positive and negative monopoles are found for statistically equivalent vorticity fields. The dashed line in Fig. 9 corresponds to dipolar solutions of the linearized equations. In Ref. [19] it is shown that these fields are at best saddle points instead of entropy maxima, and, therefore, these solutions are unstable. This observation is consistent with the fact that no dipolar structures are predicted from $t=1$ in our statistical analysis. Finally, we remark that monopolar statistical equilibria are also predicted by the statistical-mechanical theory based on a pointwise discretization. Solving the sinh-Poisson equation

on a bounded square domain, Pointin and Lundgren [16] found that solutions with the highest values of the entropy have a monopolar topology.

C. Predictions from later times

We anticipate that the failure of the statistical predictions from the vorticity fields at $t=1$ is related to viscous effects in the Navier-Stokes simulations. As was shown in Fig. 6, the energy, which is conserved in the statistical theory, decays substantially in the numerical integrations. Nevertheless, by repeating the maximum entropy calculations at $t=1$ for the same discretized initial distributions, but with smaller values of E_0, we have found that this parameter does not change the global shape of the solutions. Apart from decreasing the kinetic energy, viscous dissipation leads to rapid changes in the vorticity distribution $g(\sigma)$ in the early stages of the flow evolution (see Fig. 7). In Ref. [14] it was shown that this effect is responsible for the limited applicability of the statistical theory in the case of small-scale initial conditions and periodic boundary conditions.

If changes in the vorticity distribution are responsible for the failure of the statistical theory at $t=1$, we expect to obtain increasingly better results when the statistical equilibria are computed with the constraint values E_0 and $g_0(\sigma)$ taken from later times. To verify this, we have calculated the statistical equilibria on the basis of the vorticity fields $\omega(\mathbf{r},t)$ at different times t with $1\leqslant t\leqslant 40$, for all 16 runs. The results of this analysis are illustrated by the exemplary dipole and monopole formations of Figs. 1 and 2. Figures 10 and 12 display four statistical equilibria corresponding to these respective simulations. As a first observation, notice that, indeed, the time evolution of the input parameters results in the prediction of different statistical equilibria from different times for the same run.

Let us first consider the dipole formation in more detail. For $t<12$, the statistical theory falsely predicts a monopolar quasistationary state. For example, Figs. 10(a) and 10(b) display the monopoles computed from the fields at $t=1$ and $t=6$, respectively, which are of opposite sign. For $t\geqslant 12$, a dipolar structure is predicted, as illustrated by the predictions at $t=12$ and $t=18$ in Figs. 10(c) and 10(d). Although the global shape of these latter predictions coincides with the global shape of the quasistationary state of the Navier-Stokes simulations, a detailed comparison between the vorticity plots shown in Figs. 10(c) and 10(d) and the quasistationary state of the Navier-Stokes simulation [Fig. 1(e)] still reveals differences. This can be seen clearly in Fig. 11, which contains the ω-ψ relations of the four solutions shown in Fig. 10 (solid lines), together with the ω-ψ scatter plot of the quasistationary state of the corresponding Navier-Stokes integration at $t=25$. Notice that the scatter has not yet collapsed to a functional relation, indicating that the structure is, in fact, not completely stationary. The shift of the ω-ψ curves observed in Fig. 11 reflects the structure of the solutions: the dipolar states are centered around $\psi=0$ ($t=12$ and $t=18$), whereas the curves for the negative ($t=1$) and positive ($t=6$) monopoles are situated at negative and positive values of ψ (with $\psi|_b=0$), respectively. As we have discussed above, the early time prediction of a monopolar structure (at $t<12$) is consistent with the analysis of statistical equilibria

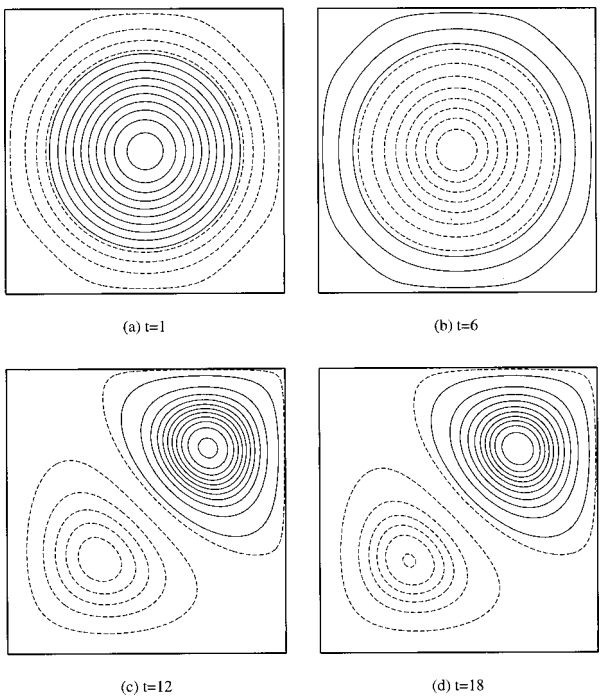

FIG. 10. Vorticity contour plots corresponding to the statistical equilibria calculated with the constraint values E and $g(\sigma)$ taken from the fields shown in Figs. 1(a)–1(d). Dashed contours represent positive vorticity, solid contours represent negative vorticity. The contour interval is 0.5 for all displayed fields.

in a linear ω-ψ approximation. The fact that, at later times, dipolar solutions are generated, implies that after a certain time the linear approximation is no longer valid. Indeed we find that the ω-ψ relation of the statistical equilibrium becomes increasingly nonlinear, as illustrated in Fig. 11. The evolution from linear to nonlinear ω-ψ relations turns out to be generic for all monopole and dipole formations.

Figure 12 contains the statistical equilibria corresponding to the formation of the monopole depicted in Fig. 2. These maximum entropy solutions have the following structures: a

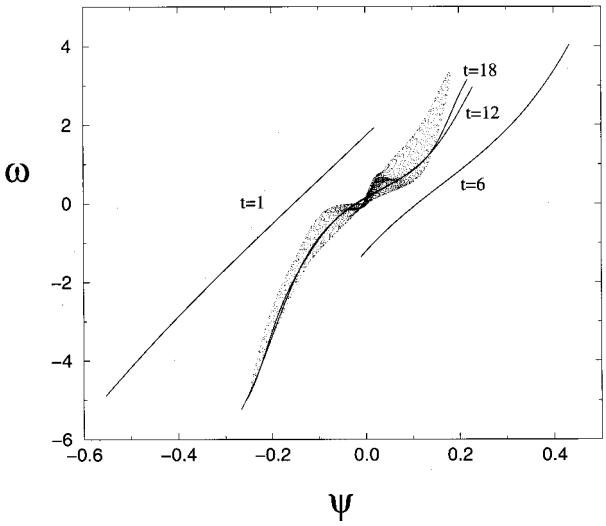

FIG. 11. ω-ψ relations corresponding to the statistical equilibria shown in Fig. 10 (solid lines), together with the ω-ψ scatter plot of the field at $t=25$ in the Navier-Stokes evolution [Fig. 1(e)].

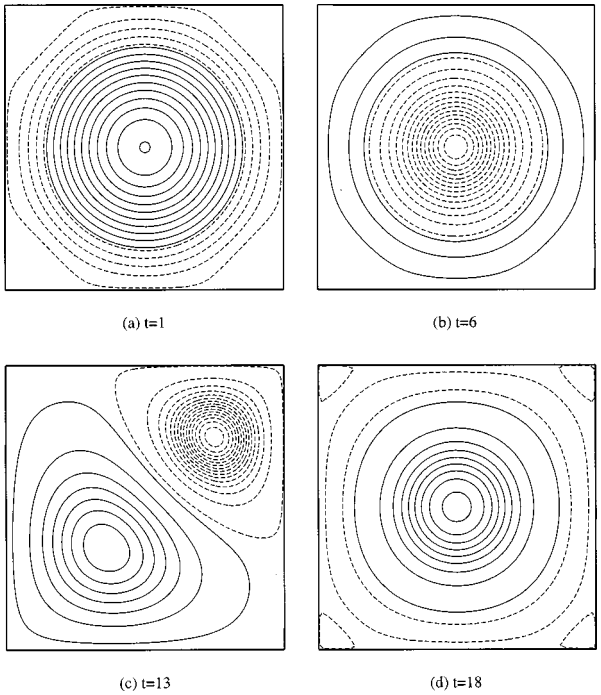

FIG. 12. Vorticity contour plots corresponding to the statistical equilibria calculated with the constraint values E and $g(\sigma)$ taken from the fields shown in Figs. 2(a)–2(d). Dashed contours represent positive vorticity, solid contours represent negative vorticity. The contour interval is 0.5 for all displayed fields.

negative monopole at $t=1$, a positive monopole at $t=6$, a dipole at $t=13$, and again a negative monopole at $t=18$. The corresponding ω-ψ relations are drawn in Fig. 13 (solid lines), together with the ω-ψ scatter plot of the quasistationary state of the corresponding Navier-Stokes integration at $t=38$. Again, after some time ($t \geqslant 14$), the global shape of the statistical prediction (a negative monopole) is in agreement with the quasistationary structure obtained in the Navier-Stokes simulation [see Fig. 2(e)]. One could argue that this structure is also predicted from the input parameters

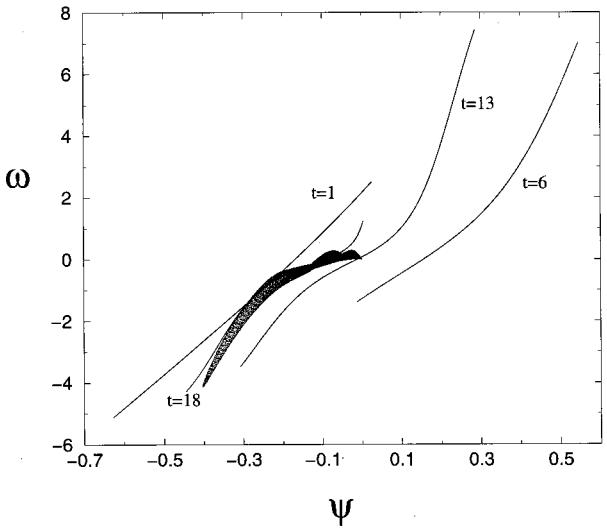

FIG. 13. ω-ψ relations corresponding to the statistical equilibria shown in Fig. 12 (solid lines), together with the ω-ψ scatter plot of the field at $t=38$ in the Navier-Stokes evolution [Fig. 2(e)].

TABLE I. Several characteristics of the reported ensemble of runs: the time at which a quasistationary state (QSS) emerges in the Navier-Stokes simulation (t_{QSS}), the type of QSS (M=monopole, D=dipole), the net circulation Γ at time t_{QSS}, the time at which the correct global structure is predicted by the statistical theory (t_{SM}), and the value of the parameter Λ at the time t_{SM}.

Run	t_{QSS}	Type of QSS	$\Gamma(t_{\mathrm{QSS}})$	t_{SM}	Λ (t_{SM})
1	24	D	0.14	12	0.38
2	38	M	−1.84	14	−0.69
3	41	D	0.04	40	0.06
4	23	D	0.63	25	0.92
	54	M	1.38	30	1.07
5	50	D	0.73	-	(1.51)
6	25	D	−0.26	20	−0.32
7	22	D	−0.15	19	−0.25
8	22	D	0.60	20	0.71
9	25	D	−0.08	10	−0.002
10	50	D	0.71	-	(1.26)
11	30	D	0.30	20	0.29
12	20	D	−0.10	15	−0.11
13	28	D	−0.12	20	−0.22
	87	M	−0.88	-	(−1.9)
14	32	D	0.87	-	(1.21)
15	20	D	−0.05	15	0.11
	72	M	−1.10	-	(−1.86)
16	32	D	0.20	15	0.41

at $t=1$ [Fig. 12(a)]. However, since this structure is predicted from the initial conditions (at $t=1$) for all runs, and since the predictions at $t=6$ and $t=13$ in Fig. 12 have a completely different shape, we feel that this correspondence is coincidental. Moreover, as can be inferred from Fig. 13, the quasistationary state of the Navier-Stokes simulation is characterized by a strongly nonlinear ω-ψ relation, whereas the ω-ψ relation predicted from $t=1$ is linear.

Similar analyses of statistical predictions from later times in the Navier-Stokes evolution of the other 14 runs revealed that, for (almost) all runs, after some time the correct global structure of the quasistationary state is predicted. Table I contains some characteristics of all 16 runs of the ensemble: the time at which the quasistationary state is reached in the simulations (t_{QSS}), the type of quasistationary state (monopole or dipole), the net circulation of this structure at time t_{QSS}, and the time at which the global structure is correctly predicted by the statistical theory (t_{SM}). From this table one can read that quasistationary dipoles with a more or less symmetric vorticity distribution (i.e., $|\Gamma| \lesssim 0.3$) are, on average, correctly predicted for $t \approx 20$, while the quasistationary state in these runs emerges on average at $t \approx 27$. If the distribution is more asymmetric ($|\Gamma| > 0.3$) the first correct prediction is generally obtained at a later time. For three runs the (asymmetric) dipolar quasistationary state is not predicted from the input fields up to $t=50$, although by that time the Navier-Stokes evolution clearly has reached a quasistationary state.

The observation that the ω-ψ relations of the statistical predictions become increasingly nonlinear when the input values are taken from later times in the Navier-Stokes evo-

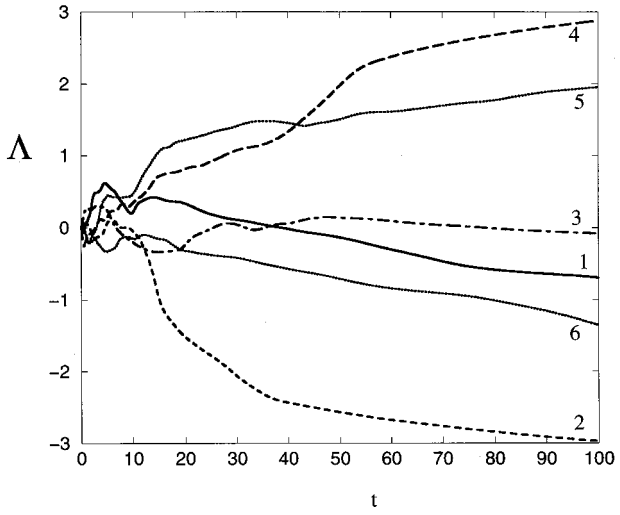

FIG. 14. Time evolution of the parameter Λ for the same runs as shown in Fig. 4. Curves 1 and 2 correspond to the runs shown in Figs. 1 and 2, respectively.

lution, implies that the vorticity distribution no longer satisfies the strong-mixing conditions. This conclusion is consistent with the fact that dipolar structures are found as stable statistical equilibria: the stability diagram corresponding to the linearized limit of the statistical theory (Fig. 9) is no longer valid. Nevertheless, it makes sense to convey some aspects of this diagram to the nonlinear regime. As discussed above, the value of $\Lambda=\Gamma/\sqrt{2E}$ determines the structure of the statistical equilibrium in the linearized limit. Although strictly speaking, this parameter is not relevant in the nonlinear regime, we find that it may serve as an indication of the structure of the predicted statistical equilibrium for a wider range of parameters. Table I contains the values of Λ at t_{SM} for all 16 runs. For those cases in which the correct global structure is not predicted for $t\leqslant 50$, the value of Λ is calculated at t_{QSS} (indicated by parentheses). In Fig. 14, the time evolution of Λ is plotted for the six simulations depicted in Fig. 4. For almost all (symmetric and asymmetric) dipole formations (curves 1, 3, and 6) in Fig. 14, $|\Lambda|$ remains relatively small for all times. In these cases, the quasistationary (dipolar) structure is well predicted by the statistical theory. Apparently, when the input parameters are sufficiently far from the regime where the linearized approximation holds, dipolar structures become stable solutions of the maximum entropy equations for $|\Lambda|<1$. In contrast, for the runs in which monopoles or strongly asymmetric dipoles are formed, $|\Lambda|$ grows significantly (curves 2, 4, and 5 in Fig. 14). Although in these cases a similar transition from the linear to the nonlinear regime occurs, for large values of $|\Lambda|$ monopoles are the only stable statistical equilibria. This observation could explain the fact that in some cases, in which the vorticity distribution is highly asymmetric, the dipolar quasistationary states are not predicted.

IV. DISCUSSION AND CONCLUSIONS

Our ensemble of Navier-Stokes simulations in a box with stress-free boundaries reveals that, for moderate values of the Reynolds number, both monopolar and dipolar quasistationary structures emerge from statistically identical initial conditions. In the statistical-mechanical analysis, based on a patchwise discretization of the continuous flow field, these structures are not predicted from the initial conditions of the simulation (at $t=1$). However, if we take the constraint values that determine the solution to the maximum entropy equations, from increasingly later times in the Navier-Stokes evolution, the global structure of the statistical prediction eventually coincides with the quasistationary state of the corresponding simulation.

In order to compare the present findings to the case of a doubly periodic domain, as described in Ref. [14], the ensemble of initial conditions presented in Sec. II has also been used in numerical simulations of 2D Navier-Stokes flow with periodic boundary conditions and Re$=2000$. (The simulations with periodic boundary conditions are performed with a Fourier pseudospectral code provided by Dr. A. Nielsen, RISØ, Denmark.) Calculating the statistical-mechanical predictions from different times in the flow evolution shows that, in the case of a doubly periodic domain, the dipolar structure of the quasistationary state is already correctly predicted from the initial condition. In the case of a bounded domain, the correct topology is predicted on a time scale comparable with the emergence of the quasistationary state.

One may expect that the statistical predictions become better if they are compared to simulations with higher values of the Reynolds number. Indeed, in Ref. [14] it was shown that for simulations with periodic boundaries and Re $=14\,000$, the precise form of the ω-ψ scatter plot is captured almost perfectly by the statistical equilibrium calculated from a relatively early time, long before the nonlinear evolution is completed. This correspondence was not found for simulations with either stress-free or periodic boundaries and Re$=2000$. In order to increase the Reynolds number in simulations on a bounded domain (with either stress-free or no-slip boundary conditions) to Re$>10\,000$, present state-of-the-art computer capacity is not sufficient. Reliable laboratory experiments on 2D decaying Navier-Stokes turbulence have not been reported for such high Reynolds numbers. Altogether, we can conclude that when comparing statistical equilibria and Navier-Stokes dynamics with either stress-free or periodic boundaries and moderate values of the Reynolds number, the predictive power of the statistical theory of vortex patches is more limited in the case of a bounded domain.

This result can be understood by recalling some characteristic properties of the Navier-Stokes evolution in the two domain types. In a finite box viscous dissipation is more substantial and is effective over a longer period than in the doubly periodic domain. In the latter case the dissipation diminishes when the small-scale structures of the initial condition have disappeared, whereas in the finite domain, small-scale structures continue to be produced when the vortices encounter the boundary and are deformed [see, for example, Fig. 1(c)]. Secondly, the applicability of statistical-mechanical theories to simulations with stress-free boundaries is limited because these boundary conditions permit net leakage of vorticity, which breaks the invariance of the circulation Γ. At early times, the sign of the net leakage appears to be a matter of chance. In most cases the net leakage remains small and results only in an asymmetry of the dipolar quasistationary state. In some cases, accidentally, the net

leakage is more substantial. When this happens, one sign of the vorticity is pushed close to the boundary and leaks out of the domain. This process enhances the growth of $|\Gamma|$, resulting in the emergence of monopolar equilibria.

Summarizing, the breakdown of the statistical predictions for the case of a box with stress-free boundaries and moderate Reynolds number is mainly due to a combination of two effects: the *viscous dissipation of the small scales* (growing kurtosis), also observed in the periodic domain, and the *net leakage of vorticity through the stress-free boundaries* (growing $|\Gamma|$). The net leakage of vorticity can be avoided by applying no-slip instead of stress-free boundary conditions, but these boundaries give rise to the production of viscous boundary layers, which are obviously not captured by the present statistical-mechanical theory. We cannot avoid the diffusion of vorticity through the boundaries by a so-called ''no-flux'' condition $(\hat{n}\cdot\nabla\omega|_b=0)$, since this condition is mathematically inconsistent with vorticity equation (1). In order to decrease the effects of viscous dissipation one could start the evolution with initial conditions, which contain less small-scale structures. However, this leads to the problem of nonergodicity in the statistical analysis [15], which we have avoided here.

ACKNOWLEDGMENTS

The authors gratefully acknowledge Professor G. J. F. van Heijst, Dr. R. A. Pasmanter, Professor H. W. Capel, and Dr. P-H. Chavanis for a number of useful discussions, and Dr. A. Nielsen for providing the numerical code to perform simulations with periodic boundary conditions. This work was performed as a part of the priority program on nonlinear systems, and as a part of the research program of the Netherlands Geosciences Foundation (GOA), both with financial aid from the Netherlands Organization for Scientific Research (NWO).

[1] E. J. Hopfinger and G. J. F. van Heijst, Annu. Rev. Fluid Mech. **25**, 241 (1993).
[2] J. A. van de Konijnenberg, J. B. Flór, and G. J. F. van Heijst, Phys. Fluids **10**, 595 (1998).
[3] D. Marteau, O. Cardoso, and P. Tabeling, Phys. Rev. E **51**, 5124 (1995).
[4] X. P. Huang and C. F. Driscoll, Phys. Rev. Lett. **72**, 2187 (1994).
[5] W. H. Matthaeus and D. Montgomery, Ann. (N.Y.) Acad. Sci. **357**, 203 (1980).
[6] J. C. McWilliams, J. Fluid Mech. **146**, 21 (1984).
[7] W. H. Matthaeus, W. T. Stribling, D. Martinez, S. Oughton, and D. Montgomery, Physica D **51**, 531 (1991).
[8] L. Onsager, Nuovo Cimento Suppl. **6**, 279 (1949).
[9] G. Joyce and D. Montgomery, Plasma Phys. **10**, 107 (1973).
[10] J. Miller, Phys. Rev. Lett. **65**, 2137 (1990).
[11] R. Robert and J. Sommeria, J. Fluid Mech. **229**, 291 (1991).
[12] J. Sommeria, C. Staquet, and R. Robert, J. Fluid Mech. **233**, 661 (1991).
[13] J. Sommeria, in *Modeling of Oceanic Vortices*, edited by G. J. F. van Heijst (North-Holland, Amsterdam, 1994).
[14] H. Brands, J. Stulemeyer, R. A. Pasmanter, and T. J. Schep, Phys. Fluids **9**, 2815 (1997).
[15] H. Brands, P-H. Chavanis, R. A. Pasmanter, and J. Sommeria, Phys. Fluids (to be published).
[16] Y. B. Pointin and T. S. Lundgren, Phys. Fluids **19**, 1459 (1976).
[17] A. C. Ting, H. H. Chen, and Y. C. Lee, Physica D **26**, 37 (1987).
[18] B. Jüttner, A. Thess, and J. Sommeria, Phys. Fluids **7**, 2108 (1995).
[19] P-H. Chavanis and J. Sommeria, J. Fluid Mech. **314**, 267 (1996).
[20] B. Jüttner, D. Marteau, P. Tabeling, and A. Thess, Phys. Rev. E **55**, 5479 (1997).
[21] S. Li, D. Montgomery, and W. B. Jones, Theor. Comput. Fluid Dyn. **9**, 167 (1997).
[22] H. J. H. Clercx, S. R. Maassen, and G. J. F. van Heijst, Phys. Fluids **11**, 611 (1999).
[23] H. J. H. Clercx, S. R. Maassen, and G. J. F. van Heijst, Phys. Rev. Lett. **80**, 5129 (1998).
[24] H. J. H. Clercx, J. Comput. Phys. **137**, 186 (1997).
[25] Y. Kondoh, M. Yoshizawa, A. Nakano, and T. Yabe, Phys. Rev. E **54**, 3017 (1996).
[26] R. H. Kraichnan and D. Montgomery, Rep. Prog. Phys. **43**, 547 (1980).
[27] B. Turkington and N. Whitaker, SIAM J. Comput. **17**, 1414 (1996).